Nanoscale domain wall devices with magnetic tunnel junction read and write

Nanoscale domain wall devices with magnetic tunnel junction read and write

E. Raymenants[1,2,a,*], O. Bultynck[1,2,a], D. Wan[1], T. Devolder[3], K. Garello[1], L. Souriau[1], A. Thiam[1], D. Tsvetanova[1], Y. Canvel[1], D. E. Nikonov[4], I. A. Young[4], M. Heyns[1,2], B. Soree[1,2], I. Asselberghs[1], I. Radu[1], S. Couet[1], V.D. Nguyen[1,*]

[1] IMEC, Kapeldreef 75, B-3001 Leuven, Belgium

[2] KU Leuven, Kasteelpark Arenberg 44 - box 2450, B-3001 Leuven

[3] Universite Paris-Saclay, CNRS, Centre de Nanosciences et de Nanotechnologies, 91120, Palaiseau, France

[4] Components Research, Intel Corporation, Hillsboro, OR 97124 USA

[a] These authors contributed equally

[*] Corresponding authors: eline.raymenants@imec.be, van.dai.nguyen@imec.be

Fast domain wall (DW) motion in magnetic nanostructures is crucial for future spintronic device concepts. However, a lack of energy-efficient, scalable and industry-relevant ways to electrically read and write DWs in nanoscale devices impedes practical applications. Here, we demonstrate that full electrical control of DW devices can be achieved by incorporating typical high DW velocity materials (i.e., Pt/Co and synthetic antiferromagnetic (SAF) Pt/Co/Ru/Co) into perpendicular magnetic tunnel junctions (pMTJs). We first show tunneling magnetoresistance (TMR) readout and efficient spin transfer torque (STT) writing, comparable to current STT-MRAM technology. Based on time-resolved measurements, we find faster STT switching dynamics in the SAF-based hybrid free layer than in conventional dual-MgO free layer while maintaining retention stability. We demonstrate the full operation of DW devices at nanoscale with MTJs enabling electrical read and write, and a heavy metal enabling spin orbit torque (SOT)-driven DW motion for information transmission. Beside implications to technology and applications, we show that these devices can be used as a tool to explore the physics of DW dynamics at nanoscale. Furthermore, using a SAF-based DW conduit has the potential to enhance device performance with faster and more reliable DW motion. This proof-of-concept offers a pathway to the technological development of high-performance and low-power DW-based devices.

Magnetic domain walls (DW) could form a key ingredient in next generation logic and data storage devices [1, 2] such as racetrack memory [3, 4], spin logic [5, 6, 7, 8] and neuromorphic computing [9, 10, 11]. The discovery of high DW velocity governed by the Dzyaloshinskii-Moriya interaction (DMI) and spin-orbit torque (SOT) [12,13,14,15] in ultrathin magnetic layers on heavy metals, the additional exchange coupling torque (ECT) in synthetic antiferromagnetic (SAF) systems [16] and the angular momentum compensation in ferrimagnets [17], were major breakthroughs in the development of fast, high density, and low-energy devices based on DW motion. To enable these materials for practical application, DWs are required to be efficiently written and read at the nanoscale. However, to date, writing of DWs has mainly been performed through magnetic field-based approaches, and read out through either Hall bar devices or magnetic imaging techniques [5, 8, 9, 12, 13, 17, 14]. These schemes play a crucial role in characterizing material properties, but their applicability

to DW devices at nanoscale is limited. Therefore, finding energy-efficient ways to electrically write and read DWs is a necessity for practical applications.

In this context, the magnetic tunnel junction (MTJ) can be considered as an excellent candidate. Indeed, current spin-transfer-torque magnetic random-access memory (STT-MRAM) technology has demonstrated that MTJs composed of a CoFeB/MgO-based free layer (FL) [18] offer uniquely high TMR readout and low STT writing current. However, the CoFeB/MgO approach faces significant challenges that relate to low DW speed [19] and poor manufacturability [20,21] for a DW conduit (Suppl. Mater. 2.2.).

In this study, we present functional DW devices with MTJs enabling electrical read and write using the hybrid free layer (HFL) design concept [22], allowing us to incorporate two well-known high DW velocity materials, *i.e.*, Pt/Co (PtCo-HFL) [12,15], and Pt/Co/Ru/Co where the thickness of Ru is varied to form a SAF- or synthetic ferromagnet (SFM)-based FL, SAF-HFL and SFM-HFL respectively [16, 23]. The HFL design offers a practical solution for the integration process and etch challenges of DW devices in industrial platforms (Suppl. Mater. 2.2.2) [21]. We validate that single MTJs with a HFL stack offer reliable TMR readout signal and efficient STT writing and could therefore be applied as inputs and outputs of a DW device. By time-resolved conductance measurements in single MTJs, we find that the Pt/Co/Ru/Co-based free layer with antiferromagnetic coupling (SAF-HFL) provides faster STT-driven switching dynamics compared to a dual-MgO reference stack. In fully integrated DW devices, we show that DWs can be locally nucleated by STT at input-MTJs and read out by TMR at output-MTJs while the DWs are directionally transported by SOT between input and output. Therefore, we demonstrate full control of a DW device, which can then be used to access both field- and SOT-driven DW dynamics at the nanoscale. Finally, we show that the HFL device proposal offers the possibility to improve DW device performance by selecting a SAF-based DW conduit.

Hybrid free layer MTJ stack design for DW-based devices

In the HFL concept, the first FL (FL1) consists of the conventional CoFeB/MgO-based FL, Fig. 1 **a**. The second FL (FL2), deposited onto a heavy metal (HM), serves as the DW conduit which typically consists of a ferromagnet [12], or a SAF-system [16]. FL2 offers high DW speed originating from interfacial DMI, SOT [12, 13, 14, 15] and/or ECT [16]. Note that the spacer material between FL1 and FL2 plays an important role in the stack design. Firstly, it serves to decouple the crystallization of CoFeB (FL1) and FL2 as the fcc (111) crystal structure of Co is incompatible with the bcc (001) crystal structure of CoFeB. Secondly, it enables ferromagnetic

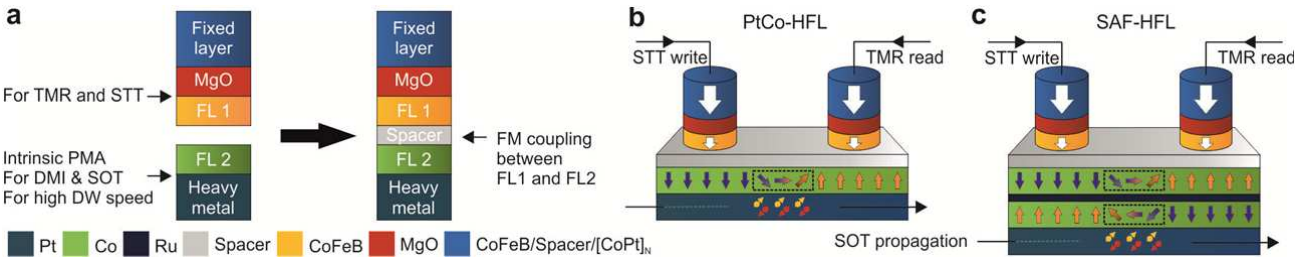

Fig. 1 | Schematic of hybrid free layer concept. (**a**) Hybrid free layer (HFL) concept consisting of FL1 (top-left), based on CoFeB/MgO for efficient STT write and high TMR read, and FL2 (bottom-left), consisting of a material with inherent perpendicular magnetic anisotropy (PMA) which is optimized for high DW velocity driven by SOT. The two free layers are ferromagnetically coupled through a spacer layer (right). (**b-c**) Schematic of DW-based devices with PtCo-HFL and SAF-HFL design, respectively. FL2 consists of a Co layer on top of Pt (PtCo-HFL) or of a Co/Ru/Co structure with SFM or SAF coupling, on top of Pt (SFM-HFL or SAF-HFL).

coupling between FL1 and FL2 by interlayer exchange coupling, so they behave as a single FL. Additionally, direct growth of an MgO tunneling barrier with bcc (001) crystal structure on Co (FL2) is not trivial due to incompatible crystal structure and poor electron band matching [22]. Therefore, incorporation of the CoFeB layer (FL1) in contact with the MgO barrier is indispensable for retaining high TMR [22, 24] and high STT switching efficiency. In principle, this approach opens the possibility of integrating any high DW speed material in FL2, including ferrimagnets [25], for specific applications such as DW or skyrmion tracks [26,27].

Fig. 1 **b-c** illustrate the device concept with Pt/Co and Pt/Co/Ru/Co as DW conduits and MTJs as write and read components. In this proposal, the DW device has three main components in which each one owns its specific functionality: DW writing (*input*), DW transport (*conduit*) and DW reading (*output*). The operation principle is as follows: STT is locally applied at the input pillar to inject DWs into the DW conduit (*i. e.,* DW

writing process) via the strong ferromagnetic coupling between CoFeB and FL2 (Extended Data Fig. 1 **a**). Subsequently, the DW travels along the track driven by magnetic field or SOT (Extended Data Fig. 1 **b**) (*i.e.,* DW transport process). The detection of the DW at the output is enabled by TMR (*i.e.,* DW reading process). As a result, this DW device concept simultaneously benefits from efficient STT switching, good TMR owing to the CoFeB/MgO interface, and high DW velocity, resulting from a combination of SOT, DMI and/or ECT in the DW conduit materials on heavy metals.

Optimized TMR reading and fast STT writing in single MTJ pillar

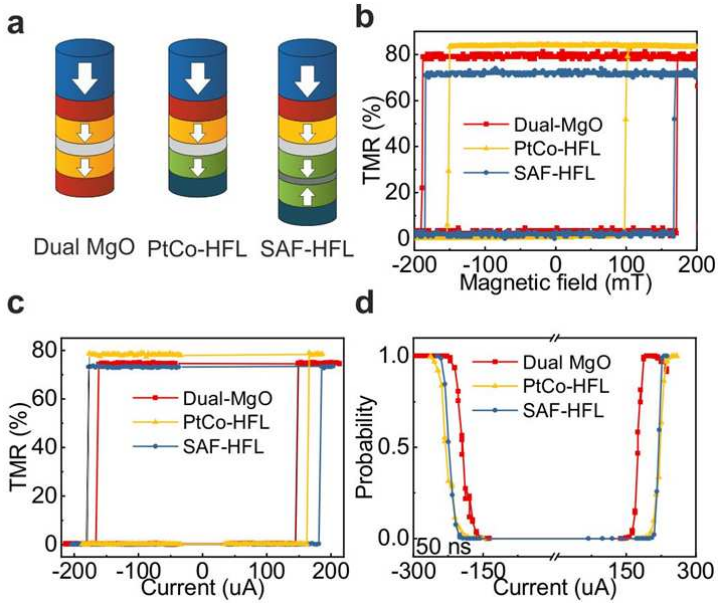

Fig. 2 | Hysteresis loops showing reliable TMR and STT in HFL-MTJs. (**a**) Illustration of standard Dual-MgO, PtCo-HFL and SAF-HFL stack, color code similar as in Fig. 1 **a**, (**b**) typical TMR loops as function of perpendicular magnetic field in MTJs with nominal diameter of 60 nm, (**c**) STT induced magnetization reversal at 50 ns pulse width, (**d**) switching probability distribution measurement averaged over 1000 events per point.

To verify the applicability of the HFL concept, we studied the magnetic properties of single MTJs made with different types of HFL (Fig. 2 **a**), fabricated on 300 mm wafers using standard processes of MRAM technology. Fig. 2 **b**-**c** display typical square TMR hysteresis loops of an MTJ pillar as function of field and current pulse, respectively. Importantly, we obtain similar TMR values, about 80 %, and STT switching currents, about 200 μA, in all types of FL. This result suggests that the obtained TMR and STT efficiency are mainly contributed by the CoFeB/MgO/CoFeB interfaces as expected in a conventional STT-MRAM device [18, 28]. Note that the lower coercivity in the PtCo- HFL device is linked to our choice of relatively low anisotropy in the stack design (Suppl. Mater. 3.2.1). The switching probability dependence of write current amplitude (Fig. 2 **d**) verifies the deterministic STT switching in all devices (Suppl. Mater. 4.3). A slightly lower write current (~ 170μA) was found in dual-MgO devices, which may be related to the lower damping constant in CoFeB [29] and dual-MgO being an already optimized stack. It is worth to note that the demonstration of good TMR read and reliable STT write in SAF-based FL design opens the path for improving DW transport as SAF systems are expected to be less sensitive to external perturbation and to show fast switching dynamics [23].

To evidence this statement, we compare magnetization switching dynamics of the SAF-HFL to a standard dual-MgO based FL using timed-resolved STT-driven switching measurements. The typical time-resolved single shot curves at room temperature, as displayed in Fig. 3 **a**, allow the extraction of three different timescales for every reversal event: the initial incubation delay t_{inc} due to thermal effects, the transition time between stable states t_{trans}, and the pinning time in a pinned state t_{pin}. For a 100 nm device size, it has been shown that the switching process is dominated by a DW-mediated reversal [30]. Note that pinning only occurs in the dual-MgO devices, as reported in Fig. 3 **b**. The varying nature of the pinning level and characteristic pinning timescale indicate that the origin is most likely due to the inhomogeneities of the device microstructure. More specifically, defects in the interfacial MgO/CoFeB anisotropy have been reported to induce pinning in the STT switching process [31].

The incubation delays were analyzed under the assumption of a thermally activated process [32] $PDF(t_{inc}) = \exp(-t_{inc}/\tau)/\tau$ where *PDF* is the probability density function. In the thermal limit for small drive currents, where the incubation delay is dominant, we expect the well-known Arrhenius dependence $\tau =$

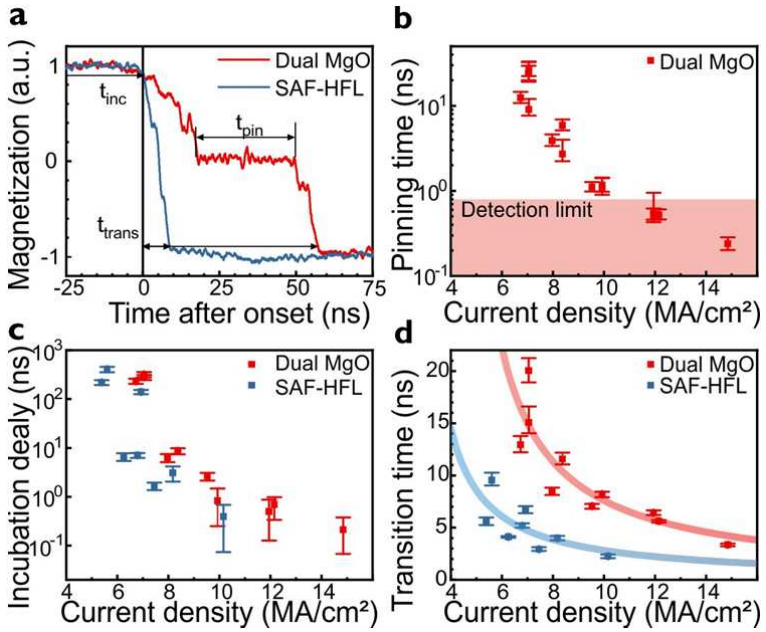

Fig. 3 | Fast STT switching in SAF-HFL without degradation of retention time. (**a**) Typical single-shot curves of the MTJ reversal process lined up to the onset of switching (time 0), defining an incubation delay, transition time, and pinning time. (**b**) Extracted characteristic pinning times, only present in the dual-MgO samples. (**c**) The thermally activated incubation delays as function of current density, demonstrating similar behavior in the two FL designs. (**d**) Transition times vary as function of current density demonstrating consistently faster reversal in the devices with the proposed SAF-HFL. Error bars in all graphs define the 68% confidence interval.

$\tau_0 \exp(\Delta[1 - J/J_c])$. However, the absence of analytical expressions for τ_0 in the DW reversal regime will prevent further parameter extraction. As displayed in Fig. 3 **c**, the similar incubation delay as function of applied current indicates similar energy barriers in both stack types (Suppl. Mater. 4.4). It is supposed that in all cases the switching process initiates in the top CoFeB layer (FL1) which is in contact with the STT source from the spin polarization layer. Subsequently, the switching of the whole FL then follows due to the strong coupling with the CoFeB layer. Interestingly, we found that the transition times in the SAF-based devices reduced by a factor of two compared to their dual-MgO counterpart as seen in Fig. 3 **d**. This result suggests that the presence of DMI and antiferromagnetic ECT [16] in our SAF-HFL devices indeed stabilize the DW configuration and lead to shorter transition times.

Full electrical operation of DW devices with MTJ write and read

We now demonstrate that a nanoscale DW device with full control can be achieved using the HFL design. In this study, DW devices with MTJs as electrical read and write components have been fabricated consisting of a 180 nm wide track shared by three MTJ pillars with a nominal diameter of 80 nm. The pillars are separated by 500 nm. We use a Co/Ru/Co FL2 as DW conduit with a 13 Å thick Ru-spacer which allows the formation of a synthetic ferromagnet, SFM-HFL. In such SFM arrangement, the thicker Ru layer ensures PMA of the bottom Co layer even when the interfacial PMA of CFB/MgO is damaged by the etching process. Importantly, the magnetic state of the DW conduit underneath and in between pillars is very similar even if the PMA of the top Co layer has collapsed by the etching process. Therefore, devices with SFM stack design can be used as demonstrators of SOT-driven DW motion where the bottom Co layer is in contact with the SOT source of Pt.

TMR versus field loops of three individual pillars connected by a common FL show the coercivity (B_C) overlapping and a significant reduction of switching field (propagation field B_P) when STT was initially applied in one of the pillars (Extended Data Fig. 2). It indicates that the PMA of the DW conduit is fully preserved after device integration [18]. This experiment demonstrates that three basic requirements for a functional DW device are guaranteed, *i.e.,* PMA of the DW conduit is preserved, DWs can be locally written in the track by STT and read out by TMR. In addition, a large difference between B_C ($\sim 61\,mT$) and B_P ($\sim 33\,mT$) provides a wide operating window for field-driven DW transport without approaching the nucleation-dominated switching regime.

We now prove, Fig. 4, that the full operation of read/write using MTJs and both field and/or SOT-driven DW motion can be achieved in a single DW device. Experimentally, the measurement sequence of a DW device with the track shared by three MTJ pillars is summarized as follows. We firstly saturate the device in the parallel (P) state by a negative external field larger than the coercivity. Consecutively, STT is used to selectively write an antiparallel (AP) domain in the center pillar P2, as seen in Fig. 4 **d-e-f** by an abrupt change of magnetization from P to AP in P2 (blue graph). Finally, the motion of DWs through the track induced by field and/or SOT is detected by TMR in the neighboring pillars. Fig. 4 **a**, **d** shows an example of field-driven DW transport in which the device is operated at a constant field of 27 mT (<< $B_C \sim 61mT$). In this case, the nucleated domain expands from the center pillar to both outer pillars driven by field and assisted by thermal activation. The result of DW motion along the track is observed by TMR read as a change of magnetic state from P to AP in both P1 and P3, demonstrating the isotropic nature of field-driven transport.

We now demonstrate that our DW devices can be operated by applying an in-plane SOT current along the track as shown in Fig. 4 **b**, **c**, **e** and **f**. In contrast to field-driven DW transport, the direction of DW motion is selectively manipulated by the current polarity. As seen in Fig. 4 **b**, **e**, we observe a change of TMR in P3 indicating DW motion from P2 to P3 with a positive current. Similarly, Fig. 4 **c**, **f** shows DW motion from P2 to P1 with negative current. Note that we never observe DW motion against the direction of current flow as no switching occurs at P3 (P1) with negative (positive) current (*c.f.*, Fig. 4 **e**, **f**). To verify the device operation reliability, we show in Extended Data Fig. 3 that the experiments are reproducible ~ 100 times.

The observation of DW motion along the current flow provides clear evidence that SOT originating from Pt is the main driving force for DW motion in our devices as expected in stand-alone samples [10-13]. In this experiment, the exact shape of the nucleated domain is not obvious since TMR readout is locally sensitive to a change of magnetization state underneath the pillars. However, we believe that a magnetic bubble was fully nucleated under the MTJ as a full switching of MTJ resistance from P to AP is always present after STT write. Also, we do not observe any change of the resistance in the neighbouring pillars during STT write meaning that a domain is locally injected underneath the MTJ. In other words, two DWs are expected to form on each side of the MTJ pillar. It is worth to mention that we do not observe two changes of resistance (*i.e.,* drop of resistance in the input pillar and rise in resistance in output pillar) as would be expected from SOT-driven DW motion (Suppl.

Mater. 6.4). It might be due to the fact that the externally applied field favors bidirectional expansion while the SOT-driven DW motion favors unidirectional motion (c.f., Fig. Suppl. 6.4). We believe that fine-tuning of the device integration process will reduce the potential DW pinning sites of the track at nanoscale such that the device can be fully controlled by SOT without external field, as we obtained in the case of stand-alone FL samples (Fig. Suppl. 6.3).

Our devices also allow to control DW motion from any pillar in the track. We show in a slightly larger device (track width 200 nm, pillar diameter 100 nm and interpillar spacing 500 nm) that SOT-driven DW motion can be achieved from any pillar where the DW is initially written by STT (Extended Data Fig. 4). This demonstration provides an important feature for practical application of spintronic devices, for instance the operation of spin logic devices which require DWs to be independently controlled from different inputs [6, 8].

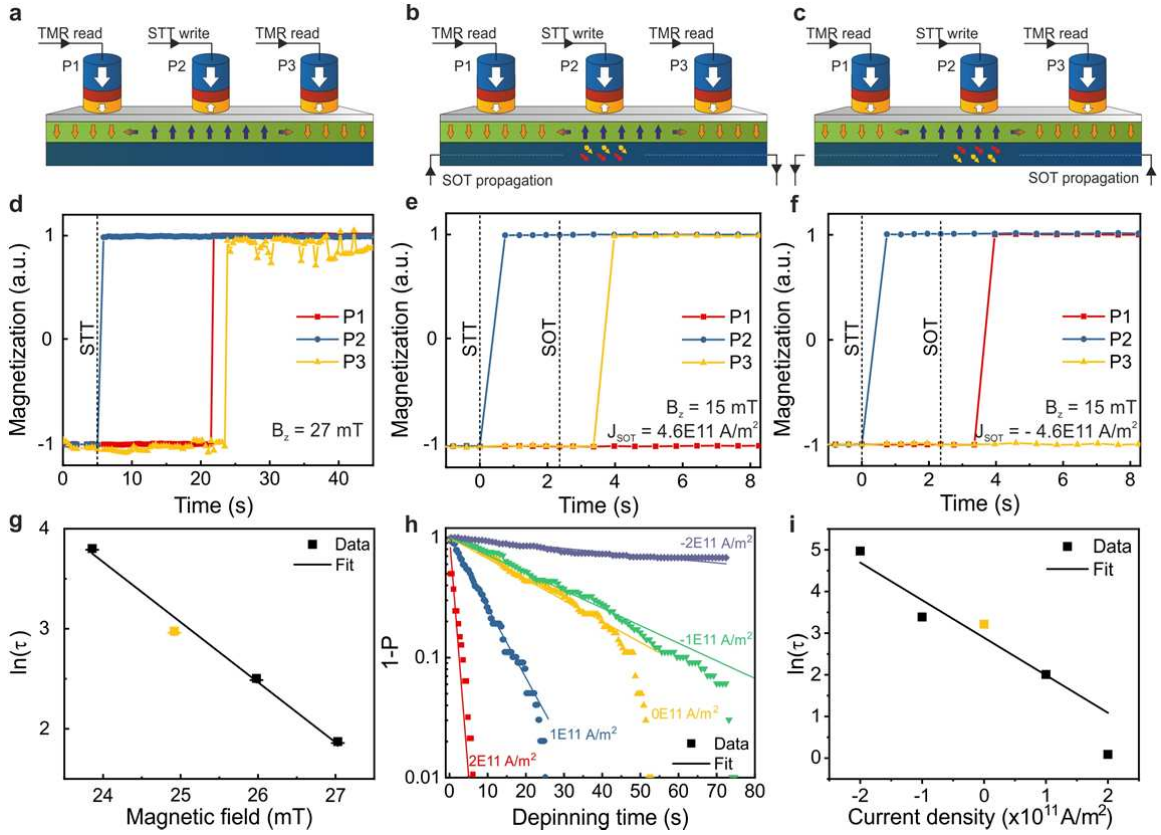

Fig. 4 | Full operation of a DW device with MTJs enabling STT write and TMR readout and SOT-driven DW transport. (**a**-**c**) Schematics explaining DW transport as observed in (**d**-**f**) respectively. (**a**,**d**) Field-driven domain expansion from P2 to both P1 and P3. (**b**, **e**) SOT-driven DW motion from P2 to P3 with positive current flow in the heavy metal and (**c**, **f**) SOT-driven transport from P2 to P1 with negative current. (**g**) Natural logarithm of the depinning time as function of external magnetic field. (**h**) Cumulative density functions (plotted as 1-CDF on logarithmic scale) of depinning time at a fixed field of 24.9 mT and varying current density obtained from 100 measurements at each current density and polarity. The data is fitted by an exponential law, resulting in the average depinning times as plotted in (**i**) as function of current.

In addition, we prove that such devices offer the possibility to explore DW dynamics in a full operation mode where imaging techniques become ineffective in fully integrated devices at low dimension. For this study, we repeat a similar experiment as seen in Fig. 4 **a** and measure the waiting time for the DW to overcome the energy barrier to travel from P2 (*i.e.*, where DW is written by STT) to P3 (*i.e.*, where DW is detected by TMR read) with the assistance of external field and thermal activation. We choose four different external field values to tune the height of the energy barrier and repeat the measurement 100 times to characterize the statistics of the depinning

time at each field value (Fig. Suppl. 6.2.1). The cumulative distribution function (CDF) of depinning time for each field value is well described by a single exponential law, $CDF(t) = 1 - exp(-t/\tau)$ with the characteristic depinning time τ, as theoretically predicted for DW depinning processes [33, 34]. Fig. 4 **g** shows the obtained τ (on ln-scale) as a function of magnetic field, fitted by an Arrhenius-law-based exponential equation $\tau = \tau_0 \exp\left(\frac{E}{k_B T}(1 - B/B_{C0})\right)$, where B_{C0} is the intrinsic critical field in the absence of thermal activation [33]. We obtain a thermal stability factor $\frac{E}{k_B T}$ of 38.8 ± 1.

Finally, we use such devices as a tool to study the impact of SOT on the DW dynamics in full operation, where the DW is electrically read and written using MTJs. We carry out similar field induced DW depinning measurements and now add SOT on top of a fixed external field of $24.9\, mT$. Fig. 4 **h** displays the CDF of depinning times (on log scale) at varying current density and polarity. As expected, a negative current increases the DW depinning time while a positive current decreases the depinning time (Fig. Suppl. 6.2.2). We find that the CDF of SOT induced DW depinning can also be fitted by a single exponential as expected for DW depinning over a single barrier. It suggests that the application of SOT does not change the nature of DW dynamics in our device. When plotting the obtained depinning time τ (on ln-scale) as function of current density (Fig. 4 **i**), we find that the effect of SOT on the DW depinning dynamics is equivalent with field-driven depinning. Therefore, we assume again an Arrhenius-law based exponential, including the effect of current $\tau = \tau_0 \exp\left(\frac{\Delta}{k_B T}\left[1 - \frac{B}{B_C} - \frac{J}{J_C}\right]\right)$ [34] and approach the effect of current similar to magnetic field. We then obtain $\tau = \tau_0 \exp\left(\frac{\Delta}{k_B T}\left[1 - \frac{B - \in J}{B_C}\right]\right)$ which allows to estimate the SOT efficiency $\in$ on the DW depinning process: $\in = 1.5 \pm 0.24\ mT \times (10^{11} Am^{-2})^{-1}$. This is in agreement with literature for PtCo-based stand-alone samples [34], which indicates that the nature of DW dynamics in the conduit layer is retained in nanoscale devices under both field and SOT-driven DW depinning.

Toward improvements of DW device performance with SAF-HFL design

The HFL proposal allows to improve device performance, for instance by integration of a SAF system as DW conduit. For this purpose, a softer etching condition in the device integration process was used. Etching was stopped in the reference layer (RL) above the MgO barrier to avoid any magnetic damage to the SAF-based DW conduit, *i.e.,* to the CoFeB/MgO interface of FL1. Note that this etch-stop condition induces an electrical short between the pillars through the RL. We believe that it does not impact the demonstration of field-driven DW motion in this study. We compare the dynamics of field-driven DW motion along PtCo-HFL and SAF-HFL conduits in a 170 nm wide track shared by three MTJs, using real-time TMR detection, Fig. 5 **a** (Suppl. Mater. 6.1). The time resolved single-shot curves in Fig. 5 **b** show a sequential switching of pillars P1, P2 and P3 under the application of the sweeping magnetic field. It suggests that at coercivity, a domain is nucleated and sequentially

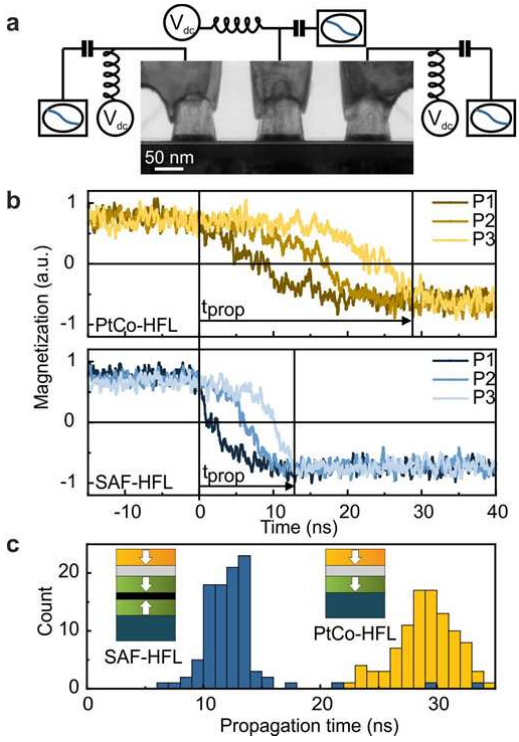

Fig. 5 | Fast DW propagation in SAF-HFL compared to PtCo-HFL. (**a**) Cross-sectional TEM image of 3 MTJs with a nominal diameter of 70 nm and interpillar spacing of 100 nm sharing the same FL. Bias tees enable individual DC and high-frequency access to each pillar. (**b**) Single-shot time-resolved field-driven magnetization reversal at coercivity in PtCo-HFL (42.5 mT) and SAF-HFL (63 mT), (**c**) Propagation time measured from 100 measurements as in **b**, showing shorter propagation time in SAF-HFL.

expanded throughout the DW conduit. This measurement reveals that the dynamics of DW motion in high DW

speed materials, more specifically in CoPt or in the Co-based SAF system, can be sensed by TMR detection in nanoscale devices. The propagation time, defined as the delay-time between the onset of reversal in P1 and the termination of reversal in P3, is at least double in PtCo-HFL (28.99 ± 2.63 ns) as compared to SAF-HFL (13.09 ± 5.48 ns). It means that DW motion in SAF-based devices with an average DW velocity of 42 m/s, is faster than in PtCo-based devices with an average DW velocity of 17 m/s. Faster DW motion in SAF is attributed to the combination of DMI and interlayer exchange coupling which helps to stabilize the DW structure during its motion thus extending the steady motion regime to larger fields compared to its ferromagnetic counterpart. Note that our SAF is not fully compensated (Fig. Suppl. 3.2.2) and that the effect of field on DW motion will be less sensitive if the SAF system is more compensated urging for SOT- rather than field-driven DW motion. Thus, we finally study SOT-driven DW motion in a stand-alone SAF-FL by Kerr microscopy. We indeed observe uniform (Suppl. Video) and fast SOT-driven motion (DW velocity up to *460 m/s* at $J = 3 \times 10^{12}$ A/m^2) in a SAF-based sample (Fig. Suppl. 6.3). This suggests that a SAF-based DW conduit could enable higher performance DW devices. Therefore, we believe that fine-tuning the MTJ stack design and improving etching conditions to ensure the PMA of the full SAF structure will be key for fast SOT-driven DW motion devices.

Conclusions

In summary, we experimentally demonstrated the full operation of a DW device using the HFL-MTJ concept which can provide all requirements for high density and low power DW-based devices including STT write, TMR read and SOT-driven DW motion. This device provides a way to study the physics of DW dynamics under both field and/or SOT at the nanoscale. Moreover, we showed that SAF-based DW conduit devices offer a significant advantage compared to their ferromagnetic counterpart thanks to the characteristic properties of antiferromagnetic materials. These include faster STT writing speed in a single MTJ device and uniform and fast DW motion in the SAF-based DW conduit devices. Therefore, in combination with an optimized manufacturing process of nanoscale devices, we believe that this HFL device concept not only leads the way towards the practical realization of DW-based devices but also shows promise for the development of other potential spintronic devices, such as skyrmion and spin-wave based devices.

1. Dieny, B. *et al.*, Opportunities and challenges for spintronics in the microelectronics industry. *Nature*

Electronics **3** (8), 446-459 (2020).

2. Manchon, A. *et al.*, Current-induced spin-orbit torques in ferromagnetic and antiferromagnetic systems. *Reviews of Modern Physics* **91** (3), 035004 (2019).
3. Parkin, S., Hayashi, M. & Thomas, L., Magnetic domain-wall racetrack memory. *Science* **320** (5873), 190-194 (2008).
4. Blasing, R. *et al.*, Magnetic Racetrack Memory: From Physics to the Cusp of Applications Within a Decade. *Proc. IEEE*, 1-19 (2020).
5. Allwood, D. A. *et al.*, Magnetic domain-wall logic. *Science* **309** (5741), 1688-1692 (2005).
6. Nikonov, D., Bourianoff, G. & Ghani, T., Proposal of a spin torque majority gate. *IEEE Elec. Dev. Lett.* **32** (8), 1128 - 1130 (2011).
7. Hu, X., Timm, A., Brigner, W. H., Incorvia, J. A. C. & Friedman, J. S., SPICE-only model for spin-transfer torque domain wall MTJ logic. *IEEE Trans. Electron Devices* **66** (6), 2817-2821 (2019).
8. Luo, Z. *et al.*, Current-driven magnetic domain-wall logic. *Nature* **579**, 214–218 (2020).
9. Siddiqui, S. *et al.*, Magnetic domain wall based synaptic and activation function generator for neuromorphic accelerators. *Nano Lett.* **20** (2), 1033-1040 (2019).
10. Grollier, J. *et al.*, Neuromorphic Spintronics. *Nat. Electron.*, 1-11 (2020).
11. Yue, K., Liu, Y., Lake, R. K. & Parker, A. C., A brain-plausible neuromorphic on-the-fly learning system implemented with magnetic domain wall analog memristors. *Sci. Adv.* **5** (4), eaau8170 (2019).
12. Miron, M. *et al.*, Fast current-induced domain-wall motion controlled by the Rashba effect. *Nat. Mater.* **10**, 419–423 (2011).
13. Emori, S., Bauer, U., Ahn, S.-M., Martinez, E. & Beach, G. S., Current-driven dynamics of chiral ferromagnetic domain walls. *Nat. Mater.* **12** (7), 611-616 (2013).
14. Avci, C. O. *et al.*, Interface-driven chiral magnetism and current-driven domain walls in insulating magnetic garnets. *Nat. Nanotechnol.* **14** (6), 561-566 (2019).
15. Thiaville, A., Rohart, S., Jue, E., Cros, V. & Fert, A., Dynamics of Dzyaloshinskii domain walls in ultrathin

magnetic films. *EPL* **100** (5), 57002 (2012).

16. Yang, S.-H., Ryu, K.-S. & Parkin, S., Domain-wall velocities of up to 750 m/s driven by exchange-coupling torque in synthetic antiferromagnets. *Nat. Nanotechnol.* **10** , 221–226 (2015).
17. Kim, K.-J. *et al.*, Fast domain wall motion in the vicinity of the angular momentum compensation temperature of ferrimagnets. *Nat. Mater.* **16** (12), 1187--1192 (2017).
18. Ikeda, S. *et al.*, A perpendicular-anisotropy CoFeB--MgO magnetic tunnel junction. *Nat. Mater.* **9**, 721-724 (2010).
19. Burrowes, C. *et al.*, Low depinning fields in Ta-CoFeB-MgO ultrathin films with perpendicular magnetic anisotropy. *App. Phys. Lett.* **103** (18), 182401 (2013).
20. Raymenants, E. *et al.*, *Scaled spintronic logic device based on domain wall motion in magnetically interconnected tunnel junctions*, presented at IEDM, 2018 (unpublished).
21. Wan, D. *et al.*, Fabrication of magnetic tunnel junctions connected through a continuous free layer to enable spin logic devices. *Jpn. J. Appl. Phys* **57** (45), 04FN01 (2018).
22. Liu, E. *et al.*, Control of interlayer exchange coupling and its impact on spin--torque switching of hybrid free layers with perpendicular magnetic anisotropy. *IEEE Trans. Magn.* **53** (11), 1-5 (2017).
23. Duine, R., Lee, K.-J., Parkin, S. S. & Stiles, M. D., Synthetic antiferromagnetic spintronics. *Nat. Phys.* **14** (3), 217–219 (2018).
24. Perrissin, N. *et al.*, A highly thermally stable sub-20 nm magnetic random-access memory based on perpendicular shape anisotropy. *Nanoscale* **10** (25), 12187 (2018).
25. Avil'es-Felix, L. *et al.*, Single-shot all-optical switching of magnetization in Tb/Co multilayer based electrodes. *Sci. Rep.* **10** (1), 1-8 (2020).
26. Legrand, W. *et al.*, Room-temperature current-induced generation and motion of sub-100 nm skyrmions. *Nat. Mater.* **19** (1), 34-42 (2020).
27. Dohi, T., DuttaGupta, S., Fukami, S. & Ohno, H., Formation and current-induced motion of synthetic antiferromagnetic skyrmion bubbles. *Nat. Commun.* **10** (1), 1-6 (2019).

28. Hirohata, A. *et al.*, Review on Spintronics: Principles and Device Applications. *J. Magn. Magn. Mater.*, 166711 (2020).

29. Devolder, T. *et al.*, Damping of CoxFe80- xB20 ultrathin films with perpendicular magnetic anisotropy. *Appl. Phys. Lett.* **102** (2), 022407 (2013).

30. Bouquin, P., Rao, S., Kar, G. S. & Devolder, T., Size dependence of spin-torque switching in perpendicular magnetic tunnel junctions. *Appl. Phys. Lett.* **113** (22), 222408 (2018).

31. Alzate, J. G. *et al.*, *2 MB array-level demonstration of STT-MRAM process and performance towards L4 cache applications*, presented at IEDM, 2019 (unpublished).

32. Brown, W. F. J., Thermal fluctuations of a single-domain particle. *Phys. Rev.* **130** (5), 1677 (1963).

33. Fukami, S., Ieda, J. & Ohno, H., Thermal stability of a magnetic domain wall in nanowires. *Phys. Rev. B* **91** (23), 235401 (2015).

34. Haazen, P. *et al.*, Domain wall depinning governed by the spin Hall effect. *Nature Materials* **12** (4), 299-303 (2013).

35. Metaxas, P. a. J. J. a. M. A. *et al.*, reep and flow regimes of magnetic domain-wall motion in ultrathin Pt/Co/Pt films with perpendicular anisotropy. *Phys. Rev. Lett.* **99** (21), 217208 (2007).

Methods

Sample fabrication: All devices were fabricated in imec's 300 mm pilot line. First, a buried bottom electrode contact (BEC) process was used to define the bottom electrode. Here, single damascene W metallization was applied two times, first to define BEC feedlines and second to define contact plugs. Next, the W contact plugs were capped by an ultra-smooth TaN seed layer prior to MTJ deposition. The stack is deposited using an ultrahigh vacuum (UHV) multitarget magnetron sputtering system at room temperature without breaking vacuum between depositions (EC7800 Canon-Anelva). Pillars were patterned by 193 nm immersion lithography and a subsequent ion-beam-etch (IBE) at normal and grazing angle for single pillar and DW devices. The DW devices required additional 193 nm immersion lithography double patterning to further define the free layer shape. Finally, dual damascene Cu top contacts were fabricated to provide electrical readout at the individual pillars. The dual

MgO FL stack, PtCo-HFL stack, SAF-HFL and SFM-HFL stack consist from bottom to top, of *$Co_{20}Fe_{60}B_{20}$(9)/Mg(6)/Ta(3)/ $Co_{20}Fe_{60}B_{20}$(11)/MgO(10)*, of *Pt(30)/Co(8)/W(3)/$Co_{20}Fe_{60}B_{20}$(8)/MgO(10)*, *Pt(30)/Co(8)/Ru(8.5)/Co(6)/W(3)/$Co_{20}Fe_{60}B_{20}$(8)/MgO(10)*, and of *Pt(30)/Co(8)/Ru(13)/Co(6)/W(3)/$Co_{20}Fe_{60}B_{20}$(8)/MgO(10)*, respectively. Thicknesses in brackets are provided in Angstrom. The magnetic hard layer (HL) consists of a $Co_{17.5}Fe_{52.5}B_{30}$ reference layer (RL) which is ferromagnetically coupled to a SAF that consists of *Co(12)/Ru(8.5)/Co(6)/Pt(8)/[Co(3)/Pt(8)]$_6$*. More information on the fabrication process can be found in [21].

Electrical setup: A detailed scheme of the electrical setup of Fig. 3 is provided in Fig. Suppl. 5.1, this setup allows time-resolved measurements of STT-driven magnetization reversal in single pillars. The measurements were performed on high-frequency capable 100 nm pillars. By applying voltage pulses of varying amplitude and short ramp time (~300 ps) we could study the magnetization dynamics down to the nanosecond regime. The magnetic offset field was compensated for by an external magnetic field during the STT-driven reversal. Prior to the recording of the single shot data, two reference traces were recorded for the P and AP state as described in Suppl. Mater. 5. The single shot data travels between the two recorded reference states, which allow the normalization of the single shot data, as shown in Fig. Suppl. 5.2. For each point in Fig. 3, 100 single shots were recorded.

The electrical setup for the DW devices in Fig. 4, consists of a source measure unit (SMU) at each pillar, allowing individual STT-writing and TMR readout in each pillar. An additional SMU is connected to the track to allow in-plane current in the heavy metal. To avoid erroneous signals during SOT-driven DW transport, SMUs at the MTJs are kept floating while a current (100 ms) is applied through the track. Consecutively, each pillar is read out.

The electrical setup in Fig. 5, consists of radiofrequency and DC paths enabled by bias tees at each pillar. A DC bias is applied at every pillar during magnetization reversal driven by field. At coercivity, the resistance of the pillar suddenly changes leading to a reflection of the applied current. The recorded rf voltages measured by the 25 GHz oscilloscope then equal the reflected rf current multiplied by the 50 Ω termination of the scope channels.

Acknowledgements This work was performed as part of the imec IIAP core CMOS program. The authors thank the P-line for operational support. The Kerr microscopy experiments were performed at Technische

Universiteit Eindhoven, the authors thank Reinoud Lavrijsen. E. R. gratefully acknowledges FWO-Vlaanderen for a Strategic Basic Research Ph.D. fellowship.

Author contributions V.D.N. and S.C. conceived the HFL device concept and managed the project. E.R. and V.D.N performed the SOT-driven DW measurements, E.R., O.B., V.D.N and T.D. performed the time-resolved experiments and interpreted the results with help of K.G., S.C., D.W., I.R., I.A, I.Y., D.N., B.S. and M.H.; Device integration was performed by D.W., Y.C., L.S., A.T. and D.T.; The thin films were deposited by S.C.; E.R., O.B., KG. and V.D.N. wrote the manuscript. All authors discussed the results and commented on the manuscript.

286 **Extended Figures**

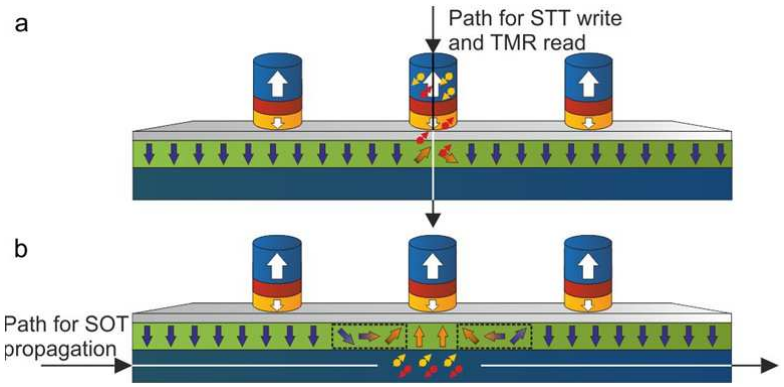

Extended Data Fig. 1 | Representation of current flow. Current path for reading and writing displayed for center pillar (**a**) and for DW motion driven by SOT (**b**).

287

288

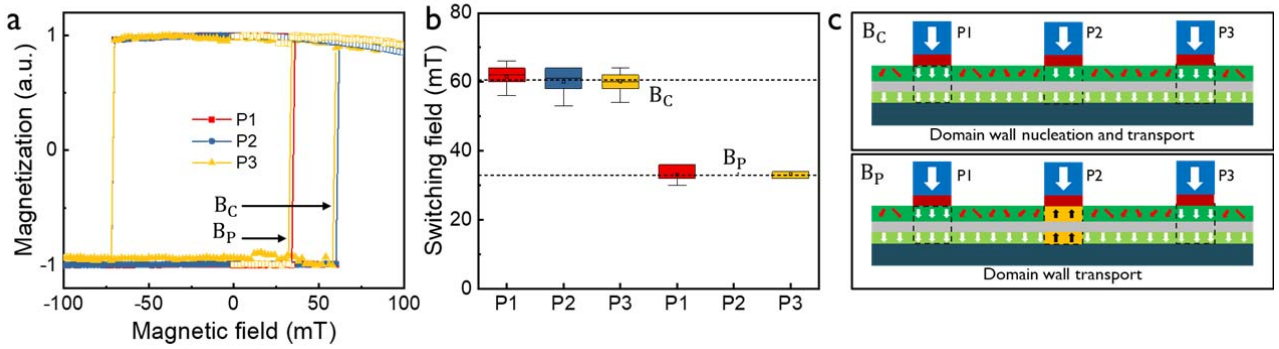

Extended Data Fig. 2 | Comparison of coercive field and propagation field. (**a**) The coercive field B_C is the switching field obtained during a conventional RH loop. The propagation field B_P is obtained after STT-driven nucleation in the center pillar (P2) and consecutive sweeping of the z-field from 0 mT upwards. The domain then expands to the outer pillars (P1 and P3). (**b**) Box plots of the coercive and propagation fields of 10 measurements. The average coercive field is 61 mT while the propagation field to both pillars is only 33 mT. (**c**) Demonstration of the initial state of the device before the RH loops is initiated. Device is fully saturated to obtain coercive field B_C (top), a domain was initially nucleated in P2 to obtain the propagation field B_P (bottom).

289

290

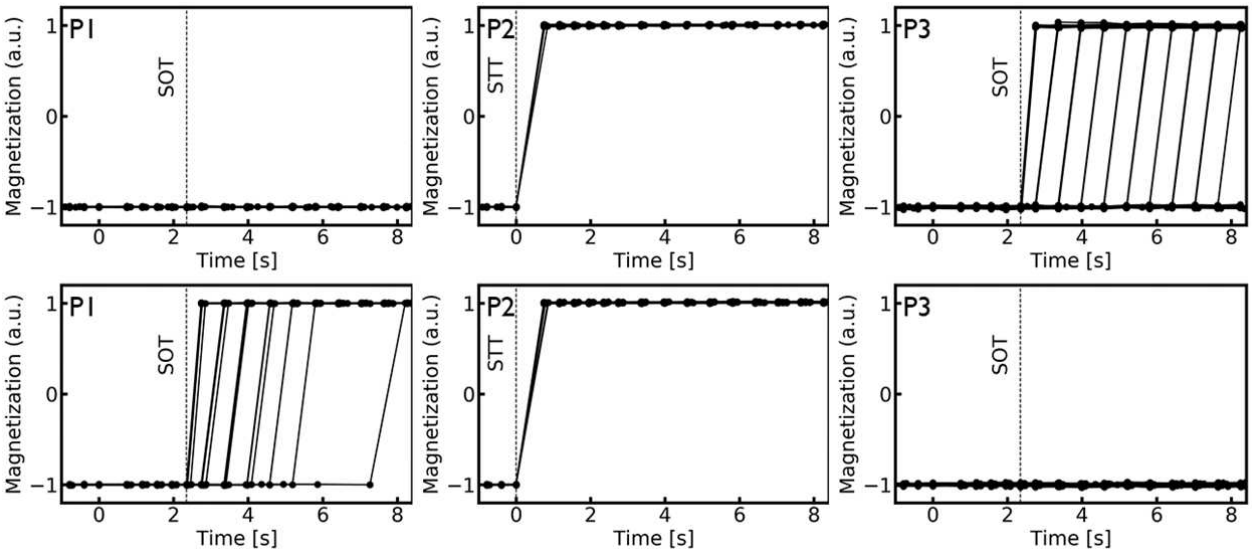

Extended Data Fig. 3 | ~100 x reproducibility of SOT-driven DW transport as in Fig. 4 e, f, STT nucleation in P2 followed by SOT-transport to P3 with positive current (top) and SOT transport to P1 with negative current (bottom). Measurement ~100 x reproducible with each current polarity. The DW never propagates to the reverse direction, i.e. no switch in P1 (top) and P3 (bottom).

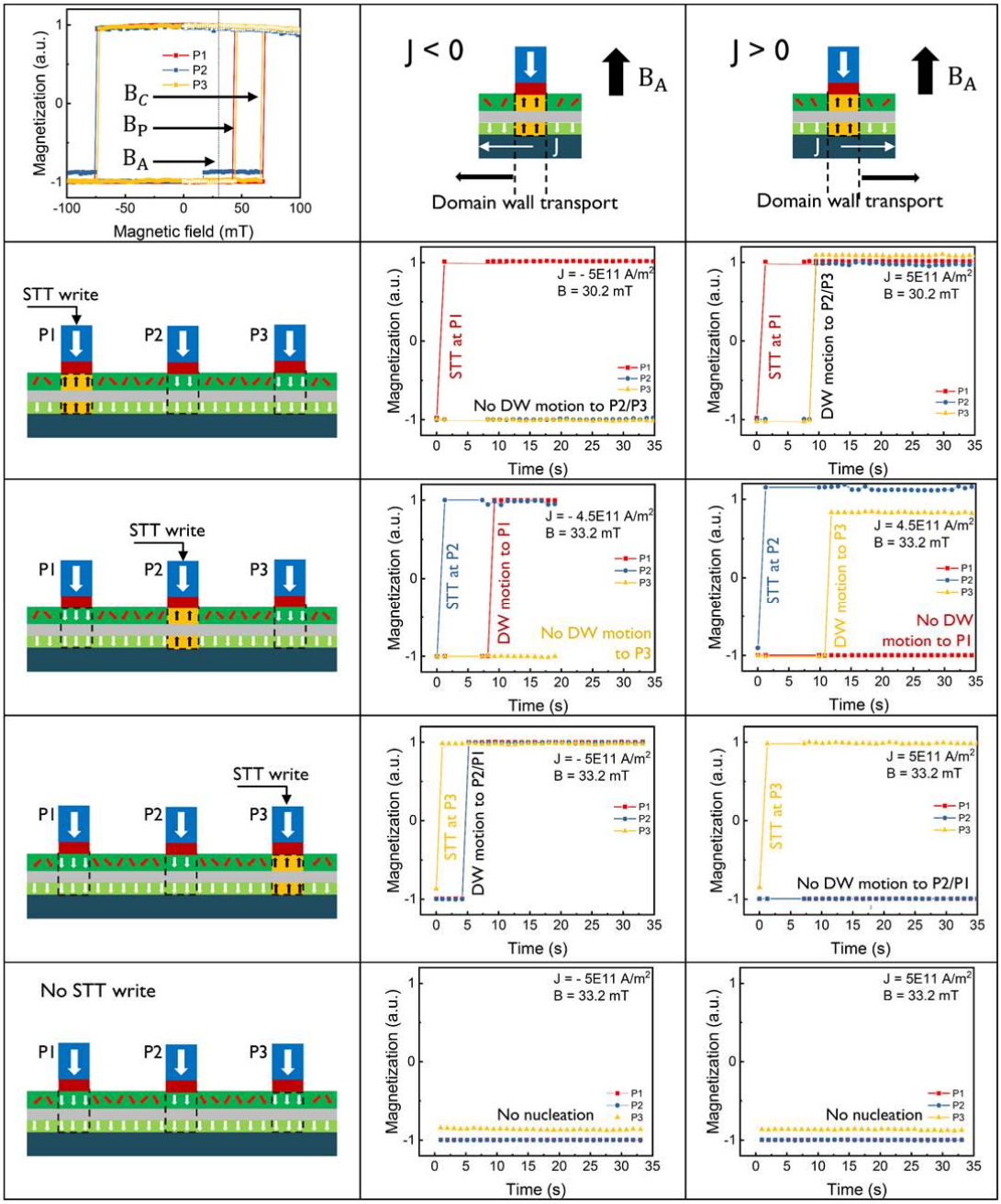

Extended Data Fig. 4 | Full demo of SOT-driven transport starting from each pillar. (Top left) Resistance versus field loop displays the coercive field B_C, the propagation field B_P and the assist field B_A for SOT-driven transport. The schematics at the top display the applied current polarity and direction of DW motion. The domain is nucleated by STT in P1 (second row), P2 (third row), and P3 (fourth row) as shown by the schematics on the left. In the last case (fifth row), no domain is nucleated by STT. The latter confirms that all the above are SOT-driven propagation of DWs, and not SOT-driven switching.

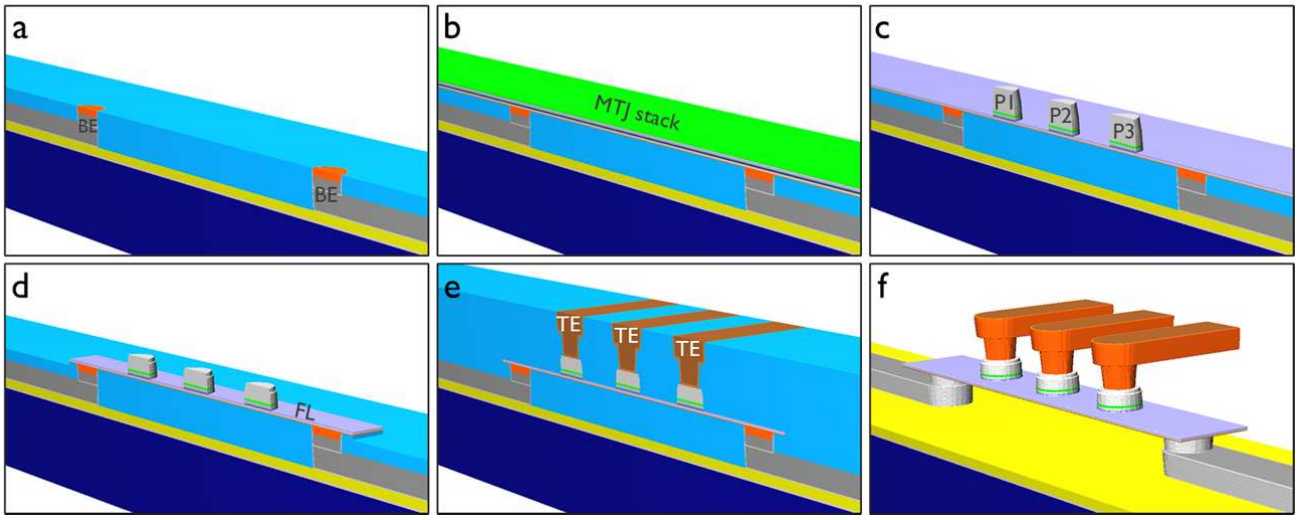

Extended Data Fig. 5 | Fabrication process in imec's 300 mm pilot line. (**a**) Bottom electrode contact (BEC), BEC feedlines and contact plugs were defined. (**b**) MTJ stack deposition using UHV magnetron sputtering system (**c**) Pillar patterning by 193 nm immersion lithography followed by ion-beam-etch (IBE) (**d**) FL shape is defined by 193 nm immersion lithography double patterning (**e**) Dual damascene Cu top contact formation (**f**) 3-dimensional image of DW device with individual TE for each pillar.